Analysis of the cathode side of a PEMFC varying design parameters to optimize current distribution and power density

T. Falagüerra, P. Muñoz, G. Correa

PII: S1572-6657(20)31049-3

DOI: https://doi.org/10.1016/j.jelechem.2020.114820

Reference: JEAC 114820

To appear in: *Journal of Electroanalytical Chemistry*

Received date: 31 August 2020

Revised date: 29 October 2020

Accepted date: 29 October 2020

Please cite this article as: T. Falagüerra, P. Muñoz and G. Correa, Analysis of the cathode side of a PEMFC varying design parameters to optimize current distribution and power density, *Journal of Electroanalytical Chemistry* (2020), https://doi.org/10.1016/j.jelechem.2020.114820

Analysis of the cathode side of a PEMFC varying design parameters to optimize current distribution and power density

T. Falagüerra[a,b], P. Muñoz[a], G. Correa[a,b,*]

[a] *Centro de Investigaciones y Transferencia de Catamarca (CITCA), CONICET-UNCA, Prado 366, K4700BDH. San Fernando del Valle de Catamarca, Catamarca, Argentina.*

[b] *Facultad de Ciencias Exactas y Naturales, Universidad Nacional de Catamarca, Av. Belgrano 300, K4700AAP, San Fernando del Valle de Catamarca, Catamarca, Argentina.*

Abstract

The amount and distribution over the active area of current density produced by the stack is a key aspect of a fuel cell performance. The performance of a proton exchange membrane fuel cell (PEMFC) is affected by many factors, including the operating conditions, flow field and manifold design, and membrane performance. In the present study, a 3D multiphysics model of a PEMFC half-cell focused in the cathode side is developed. Statistical analysis tools are proposed to quantitatively evaluate the current density distribution on the active area of the electrode in order to guarantee a proper distribution while maintaining power density. The analysis was done choosing four design parameters at three different levels on which a fractional factorial experimental design provided by the Taguchi method was applied. Finally the $0.65\,V$ working potential, that guarantees a good power generation and its adequate density current distribution on the active area of the cell, is selected. The best conditions were obtained with geometries of parallel channels, maximum gas diffusion layer porosity, maximum inlet air velocity and minimum vapor fraction, this combination improves 2.31 times the power generated in the worst case analyzed.

Keywords: Cathode PEMFC model, Statistical tools, Current distribution, Taguchi, Optimization

1. Introduction

Proton exchange membrane fuel cell (PEMFC) are electrochemical devices that convert chemical energy into electrical energy producing heat and water as a by-product. The low operating temperature, high power density, rapid start-up, and zero emissions of PEMFC stacks

* Corresponding author

Email address: correa.gabriel@conicet.gov.ar (G. Correa)

make them suitable for use in the automotive industry [1]. However, the cost and durability of PEMFC systems remain major barriers to their commercialization and market penetration [2]. Water management is of vital importance to achieve maximum performance and durability from PEMFCs. In this way flow channels play an important role among the components of a fuel cell, because they perform various essential functions that enable the system to improve water management. In most cases operating conditions have a strong contribution over the water production [3]. A higher power density is obtained as the result of a higher current density generated from the electrochemical reaction. Generally a power density increase can compromise the cell useful life, mainly due to the aging and degradation of the proton exchange membrane [4]. Moreover, the poor distribution of reactants in PEMFC flow fields leads to an uneven or non-uniform current density. This, in turn, generates localized hot spots on the membrane electrode assembly, material degradation and reduced cell performance [5]. It is desirable that reaction velocities, current density and released energy are distributed homogeneously over the entire catalytic layer and the membrane. It is well known that not all the operating parameters have the same impact over performance of the PEMFC [6].

Numerous studies describe the advantages and disadvantages for different kinds of bipolar plates and flow channel configurations, being parallel, serpentine and interdigitated geometries the most habitually studied [7–12]. Furthermore, there are many works where the impact of the variation of different parameters related to the architecture of cells are studied and optimized to improve the design of the gas flow channels [12–17]. Most of this studies mainly consider the flow field and the reactant distribution as the result [18], giving less importance to the current density generation and its distribution over the catalyst layer. This distribution is studied in various ways, although in general, it ends up expressed as a colored surface and in the best case as a data matrix. [19–22].

Solehati et al. [23] evaluated the impact of the key operating parameters of a liquid-cooled PEM fuel cell stack in its performance, efficiency, and cell lifetime to improve efficiency using waste heat for combined heat and power. Sezgin et al. [24] investigated the effect of the critical design parameters, velocities of inlet gases (hydrogen and air) and the conductivity of polymer membrane, on the performance of a high temperature PEM fuel cell in a single flow channel. However, these results are shown as surfaces with color scales and are not sufficient to infer whether one distribution is more homogeneous than another. Therefore, it is important to study the

use of analytical tools that provide a quantitative response regarding the distribution of the different parameters such as current density, temperature or reactive concentration. Kwon et al. [25] use descriptive statistics (mean, variance, kurtosis coefficient and range) to analyze the results from a PEMFC model of the distribution of hydrogen concentration on the active area of the anode, the distribution of water at the cathode and to select an operating reference voltage where a more homogeneous distribution is presented. Works by Xing et al. [26] and Xing et al. [27] analyze the distribution of current density by normalized standard deviation in a 2D model. These statisticals are applied to the data regardless of their location and environment, and are thus unable to differentiate between an continuously increasing slope of values and a surface with peaks generated by hotspots. To address the issue of inhomogeneities in a systematic manner, in the present work an index is proposed that analyzes the surface properties of the data, allowing a better understanding of its behavior. The Hydrogen Oxidation Reaction (HOR) is 100,000 times faster than Oxygen Reduction Reaction (ORR), and hence cathodic phenomena could be considered as the conditioning step for the global reaction [28], moreover most of the difficulties associated with transport phenomena usually take place in the cathode side [21]. For this reason in the present study, a single PEM half-cell 3D multiphysics model of the cathode was developed. Traditional statistical analysis tools and a novel index were used to evaluate the current density distribution on the active area of the electrode. A fractional factorial design is provided using the Taguchi method, considering three levels for each one of the following appropriately chosen design and operational parameters: channel arrangement, Gas diffusion layer (GDL) porosity, the inlet air flow velocity and its vapor fraction. The operating potential was selected using five statistical indices to evaluate the results over the active area and guarantee a smooth distribution of current density while maintaining a high power density for all simulations. Finally, the simulation results were assessed at the selected operating potential to analyze the impact of the design parameters and find the combination that offers the best distribution of current density and power.

2. Numerical model

A multi-physical model for the cathode (Flow channel, gas diffusion layer and catalyst layer) was developed and solved using the finite element method. This model involves the equations for momentum, energy conservation and mass conservation. A source term equation was used to take into account the H_2O formation and the O_2 consumption [29]. The values of the parameters used in this model are shown in Table 1.

Symbol	*Value*	*Parameter*
A_{gdl}	1250 mm^2	GDL active area
W_{rib}	0.7 mm	Rib width [30]
W_{ch}	0.8 mm	Channel width [30]
L_{plate}	50 mm	Plate length [30]
H_{ch}	0.8 mm	Channel height
H_{gdl}	0.5 mm	GDL height [30, 31]
r_{ch}	0.25 mm	Inner radius of channel corners
$E_{25\,^\circ C1\,atm}$	1.23 V	Reversible cell potential [32]
R_{ohm}	$0.285\,\Omega cm^2$	Lumped anode + membrane resistance [30]
T	343.15 K	Cell temperature
$c_{O2,ref}$	40.88 mol m^{-3}	Oxygen reference concentration
σ_{gdl}	222S m^{-1}	GDL electrical conductivity [33]
$w_{O2,in}$	0.22[illegible]	Inlet oxygen mass fraction (cathode)
μ	2.46×10^{-5} Pas	Fluid viscosity [34]
p_{ref}	101×10^{3} Pa	Reference pressure
T_A	298.15 K	Ambient temperature

Table 1: Parameters used in the half-cell PEMFC model

The cathode model domains are the distribution channel, the gas diffusion layer and the active area, which has size of $25\ mm \times 50\ mm$. The model geometry was meshed with a structured grid, the complete mesh consisted of more than 326000 domain elements and computation took 50 min in order to solve the model equations. The model inputs are: inlet air flow velocity, operational potential, species molar fraction at the inlet and GDL porosity. The model outputs are: local current density, velocity and pressure in the flow channel and molar fraction of every species in every point of the domain.

The different channel arrangements are shown in Fig. 1.

[[Image]]

Figure 1: Different channel arrangements A) Parallel B) Serpentine C) Parallel-serpentine combination

The main assumptions of the model are:

- Reactant and products are ideals gases that only exist in one phase.
- Isothermal.
- Steady state.
- Laminar flow.
- No water crossover.

This model does not take into the account the water in liquid face and thus, can be used to adequately represent the cathode behaviour medium and low power output conditions.

2.1. Mass conservation

For the gas mixtures conservation, the continuity equation for conservation of mass is considered in its differential form:

$$\frac{\partial}{\partial t}\left(\varepsilon\rho_g\right) + \nabla\left(\rho_g\vec{u}_g\right) = S_m \tag{1}$$

Where, ρ_g is the density of the gas mixture, $\vec{u}_g$ is the velocity, S_m is the source or sink of mass, ε is the porosity, which is valued as 1 in the channels. Considering ideal gases, the density of the gas mixture can be computed as an equation of state, from the mass of the gas mixture.

$$\rho_g = \frac{pMn}{RT} \tag{2}$$

Where p and T are the absolute pressure and the temperature of the system respectively, R is the universal gas constant, Mm is the mass of the gas mixture that depends on the molar fraction γ, and the molecular mass of each compound.

$$Mm = \gamma_1 Mm_1 + \gamma_2 Mm_2 + \ldots + \gamma_n Mm_n \tag{3}$$

2.2. Momentum conservation

The gravity force and electromagnetic interactions ($\vec{f}$) are considered negligible. For a fixed value of ρ and μ, the momentum equation can be simplified, obtaining the Navier-Stokes equation.

$$\frac{\partial}{\partial t}\left(\rho_g \vec{u}_g\right)+\nabla\cdot\left(\rho_g \vec{u}_g \vec{u}_g\right)=-\nabla p_g+\mu_g\nabla^2\vec{u}_g+S_u \tag{4}$$

2.3. *Species conservation*

The differential form of the conservation equation for chemical species i is presented as:

$$\frac{\partial}{\partial t}\left(\rho_g \gamma_i\right)+\nabla\cdot\left(\vec{u}_g \rho_g \gamma_i\right)=\nabla\cdot J_i+S_i \tag{5}$$

Where:

- γ_i represents the mole fraction of N_2, O_2, H_2O.
- The source or sink corresponding to the species i can be expressed as:

$$S_i=\frac{\rho_g \gamma_i \nu_i i}{nF} \tag{6}$$

- J_i is the flow corresponding to the diffusion relative to the average speed and it is expressed as:

$$J_i=D_i^{eff}\nabla\left(\rho_g \gamma_i\right) \tag{7}$$

The diffusion coefficient is obtained using the average mixing coefficients [35].

$$D_i=\frac{1-\omega_i}{\sum_{k\neq i}^{N}\frac{x_i}{D_{i,k}}} \tag{8}$$

Where N is the number of components, $D_{i,k}$ is the Maxwell-Stefan binary diffusion coefficient between species i and k, x_k is the species fraction corresponding k, ω_i is the component mass fraction of i.

For N_2-H_2O, O_2–N_2 and O_2-H_2O, the binary diffusion coefficients are:

$$D_{N_2,H_2O}=2.56\times10^{-5}\left(\frac{T}{308.1\text{K}}\right)^{1.75}\ \text{m}^2\text{s}^{-1}$$

$$D_{O_2,N_2}=2.2\times10^{-5}\left(\frac{T}{308.1\text{K}}\right)^{1.75}\ \text{m}^2\text{s}^{-1}$$

$$D_{O_2,H_2O}=2.82\times10^{-5}\left(\frac{T}{308.1\text{K}}\right)^{1.75}\ \text{m}^2\text{s}^{-1}$$

In the GDL, the effective diffusion coefficient (Eq. (9)) is affected by the porosity, which is estimated using the Bruggeman ratio [36].

$$D_i^{eff} = \varepsilon D_i^m \tag{9}$$

The species conservation in the GDL is expressed as:

$$\frac{\partial}{\partial t}\left(\varepsilon\rho_g\gamma_i\right) + \nabla\cdot\left(\vec{u}_g\rho_g\gamma_i\right) = \nabla\cdot\left(D_i^{eff}\nabla\rho_g\gamma_i\right) + S_i \tag{10}$$

2.4. Charge conservation

The electrical conduction through the GDL, is modeled using ohm's law:

$$0 = \nabla\cdot\left(\sigma_{gdl}^{eff}\nabla\phi_{ele}\right) \tag{11}$$

Where ϕ_{ele} is the electrical potential and σ_{gdl}^{eff} is the effective electrical conductivity, adjusted by the material's own porosity.

$$\sigma_{gdl}^{eff} = \left(1-\varepsilon_{gdl}\right)\sigma_{gdl} \tag{12}$$

2.5. Cathode reaction

The current density, i, is obtained from the Butler-Volmer equation. At the cathode, the electro-kinetic reaction is slow, and hence the overpotential is large, compared to the anode[37]. Therefore, the simplified Butler-Volmer equation results in:

$$i = i_0\left(\exp\left(\frac{(2-\alpha_c)F}{RT}\eta_c\right) - \left(\frac{C_{O_2}}{C_{O_2,ref}}\right)\exp\left(-\frac{\alpha_c F}{RT}\eta_c\right)\right) \tag{13}$$

Where i_0 is the exchange current density, C_{O_2} is the local oxygen molar concentration, $C_{O_2,ref}$ is the oxygen reference concentration for the oxygen reaction, α_c is the transfer coefficient of the oxygen reduction reaction at the cathode, and η_c is the cathode overpotential.

The transfer coefficient α_c is calculated as:

$$\alpha_c = \log_{10}\frac{RT}{95[\mathrm{mV}]F} \tag{14}$$

Where the cell overpotential is:

$$\eta_c = E_{cell} - E_{rev} - R_{ohm}i \tag{15}$$

3. Statistical analysis

From the data obtained solving the model, this study focuses on the values of the current density on the active area. They are presented interpolating the raw data into 50×100 matrices to keep the geometric aspect ratio. The current density values were analyzed with the statistics

described below:

The mean (Eq. (16)) is the average value of a data distribution.

$$\bar{x} = \sum_{i}^{N} \frac{x_i}{N} \tag{16}$$

The standard deviation (Eq. (17)).

$$\sigma = \sqrt{\frac{\sum_{i}^{N} \left(\bar{x} - x_i\right)}{N}} \tag{17}$$

The coefficient of variation (Eq. (18)) represents the variability of the data with respect to the mean, normalized by it.

$$CV(x) = \frac{\sigma}{\bar{x}} \tag{18}$$

The kurtosis coefficient (Eq. (19)), approaches zero for a normal distribution. Considering a kurtosis value equal to zero (0) implies that the distribution of data corresponds perfectly to the Gaussian curve of normal distribution.

$$\text{kurtosis} = \frac{\sum (x - \bar{x})^4}{(\sum (x - \bar{x})^2)^2} - 3 \tag{19}$$

Descriptive distribution statistics, such as those mentioned above, were used by others authors. Kwon et al. [25] uses them to describe the reactives distribution, [12] use standard deviation and mean of power for the optimization objective function. These statistics show how the distribution of data behaves without considering the relationship between a point of data and its surroundings.

To complement the analysis, it is proposed to incorporate the roughness index (ri), which measures the difference between a central value and its surrounding values for each current density data on the cathode active area. This generates a new matrix of values, to which the descriptive statistics (explained above) are applied. The mean of the values and their coefficient of variation give us an idea of their distribution. The ri calculation is performed according to (20), where $z_{r,c}$ is the value of current density located in row r and column c, and the root of the sum of the squared difference between the central value and its surroundings is applied.

$$ri_{r,c} = \sqrt{\sum_{i=r-1}^{r+1} \sum_{j=c-1}^{c+1} \left(z_{i,j} - z_{r,c}\right)^2} \tag{20}$$

This way, the resulting $ri_{r,c}$ are always positive values. Considering the mean of the $\overline{ri}$, it is possible to get an idea of the local variations in average, and considering the coefficient of variation of $CV(ri)$ it is evident if this variations are recurrent on the surface.

A high $\overline{ri}$ implies large local variations, on the contrary a low value implies minor variations. If the $CV(ri)$ is close to zero it is attributed to sustained variations, if it is high, it implies that the variations would not be constant. Together, both results give an idea of the current density data behavior on the active area. It would be desirable $\overline{ri}$ low with $CV(ri)$ close to zero, and a high current density.

4. Experimental design

To evaluate the current density and its distribution over cathode active area under different conditions, four parameters were selected to be modified. Each parameter was given three values, or configurations in the case of the channel arrangement, that from now on will be referred as levels. The parameters and its levels were:

- -A- Channel arrangement: parallel, serpentine and a combination of parallel and serpentine that mixes the gas flow in the curves.
- -B- GDL Porosity: 0.3, 0.4 & 0.5 (the porosity is a dimensionless quantity that takes values between 0 and 1).
- -C- Inlet air flow velocity: $1\,ms^{-1}$, $3\,ms^{-1}$ & $6\,ms^{-1}$.
- -D- vapor fraction in the inlet air flow: 0.01, 0.05 & 0.10.

Two were design parameters (channel arrangement and GDL porosity) and two of them were operating parameters (inlet air flow and vapor fraction in the inlet air flow).

For the channel arrangement, the tree proposed configurations were chosen for being the most extensively studied. Since the active area and operating temperature of fuel cell are fixed, the variation in the inlet air flow is equivalent to a modification of the cathode stoichiometric ratio. Working with the inlet air flow was favored in order to study the operating parameters from a balance of plant control point of view. The GDL porosity range selected is in line with the values usually found in literature [6, 27, 38] and the selected values for the water inlet fraction were below of those presented by [6].

The experiment was defined through a fractional factorial design inspired in a robust design [6]. The Taguchi method uses a special set of arrays called orthogonal arrays, which results

in a minimum number of experiments with maximum information about all the factors that affect the outcome. A fractional factorial design $3^{(4-2)}$ was selected. In this type of design a little amount of information is sacrificed to reduce the number of simulations. Variables are considered independent, the main effect is considerate more important than double, triple, quadruple, etc. interactions. The study was reduced from 81 to 9 simulations presented in Table 2.

Simulation	A	B	C	D
sim1111	parallel	0.3	$1\,ms^{-1}$	0.01
sim1222	parallel	0.4	$3\,ms^{-1}$	0.05
sim1333	parallel	0.5	$6\,ms^{-1}$	0.10
sim2123	paral/serp	0.3	$3\,ms^{-1}$	0.10
sim2231	paral/serp	0.4	$6\,ms^{-1}$	0.01
sim2312	paral/serp	0.5	$1\,ms^{-1}$	0.05
sim3132	serpentine	0.3	$6\,ms^{-1}$	0.05
sim3213	serpentine	0.4	$1\,ms^{-1}$	0.10
sim3321	serpentine	0.5	$3\,ms^{-1}$	0.01

Table 2: Taguchi experimental design for simulations.

For each cathode configuration defined in Table 2 the operational potential was simulated in the range from $0.5\,V$ to $0.2\,V$. An advantage of the Taguchi method is that the effect of the variation of a single design parameter in its different levels can be evaluated as the effect of the variation of the remaining parameters is compensated [39].

5. Results and discussion

To find the operating conditions that guarantee a smooth distribution of current density while maintaining a high power density for all the simulations, five descriptive statistic indices were analyzed:

- Coefficient of variation of the current density ($CV(i)$), where a value close to zero is sought, as this means less dispersion of data around the mean.
- Mean of the roughness index ($\overline{ri}$), that relates to the average variation in current density from one point of the active area and its surroundings. A lower value indicates

a smother current density distribution.

- Coefficient of variation of the roughness index ($CV(ri)$). A value close to zero is desired as it indicate a lower dispersion of the values of the roughness index.
- Kurtosis of the current density, in which case, a lower value is better.
- Average power density ($\bar{p}$), where a higher value is better.

Two of this indices, $\bar{ri}$ & $CV(ri)$, were used to understand the smoothness of the local current density distribution; and the other two, $CV(i)$ & Kurtosis, were used to compare with others studies as presented in the previous section. $\bar{p}$ was selected as another operation indices, besides the current density, to evaluate the performance of the cell under different configurations. In order to find a compromise solution between the a smooth distribution of current density in the active area and the power generated, the average power density ($\bar{p}$) and the roughness index ($\bar{ri}$) were highlighted as critical statistic indices; and the other three statistics will be used to compare simulations results.

5.1. Cell operating potential selection

The selection of the operating voltage entails a trade-off between the maximum cell power and a smooth distribution of the current density.

Fig. 2 shows the polarization curves (operating potential as a function of current density) for all the simulations carried out. This figure clearly shows how at low Inlet air flow velocity (*sim1111*, *sim2312* and *sim3213*), for voltages lower than $0.6\,\mathrm{V}$, the current remains constant. This is due to the exhaustion of the O_2 entering the cell. Decreasing the potential with the same generated current density implies a decrease in power density. Moreover, it can be seen that a higher porosity favors the increase of the generated current density, in accordance with the results obtained by Kermani et al. [38] and Huang et al. [40]. This is because the gases reach the catalytic layer more easily favoring the reaction.

[[Image]]

Figure 2: Polarization curve and power vs. current density for all simulations.

[[Image]]

Figure 3: Statistic indices for different channel arrangements A) Roughness index coefficient of variation B) Roughness index mean C) Kurtosis D) Current density coefficient of variation

Fig. 3A shows that, for all the channel configurations (A1, A2, A3), when the potential

decreases below $0.65\,V$, the mean of the roughness index increases showing a less homogeneous distribution with the increased current density. In the $\overline{ri}$ and $CV(ri)$ case (Fig. 3A and Fig. 3B), its lowest values are presented in the parallel channels arrangement. In Fig. 3C and Fig. 3D it can be seen that the kurtosis and the coefficient of variation have lower values for the parallel channel geometry. With this analysis it is evident that the best distribution is presented for the geometry of parallel channels.

Fig. 4A and Fig. 4B show that at potentials lower than $0.65\,V$ the $\overline{ri}$ and $CV(ri)$ increase their value, indicating a less homogeneous distribution with increasing current density. Fig. 4C indicates that worse kurtosis indices correspond to lower porosity, differing from Fig. 4D where the best distribution correspond to lower porosity level

[[Image]]

Figure 4: Statistic indices for different porosity levels A) Roughness index coefficient of variation B) Roughness index mean C) Kurtosis. D) Current density coefficient of variation

Fig. 5 shows the statistic indices related to the current density distribution at the active area, for the three velocity levels at different operating potential. It can be seen that a higher level of velocity is better to improve the distribution of current density. Lower inlet air flow velocities have a worse distribution. This may be due to the fact that when the O_2 is depleted, high values of current density appear at the first sections of the distribution channels, falling to zero where the O_2 is already depleted.

[[Image]]

Figure 5: Statistic indices for different inlet air flow velocity levels A) Roughness index coefficient of variation B) Roughness index mean C) Kurtosis. D) Current density coefficient of variation

In Fig. 6A, it can be seen that the index $CV(ri)$ follows a similar trend in the three defined levels when the cell potential is increased, being a water molar fraction of 0.01 the one that shows the lowest values. In Fig. 6B, a lower vapor fraction results in lower $\overline{ri}$ values. The kurtosis coefficient (Fig. 6C) shows that a lower vapor fraction (D1) has a value close to -1 which reflects a more even distribution of current density over the active area. In Fig. 6D, the $CV(i)$ shows that a lower dispersion in the data is found for the lowest value of water molar fraction.

[[Image]]

Figure 6: Statistic indices for different vapor fraction levels in the inlet air flow A) Roughness

index coefficient of variation B) Roughness index mean. C) Kurtosis D) Current density coefficient of variation

From the previously observed data, it can be highlighted that from $0.90\,\mathrm{V}$ to $0.65\,\mathrm{V}$ the values of statistic indices are maintained with some stability within a desired range, and that from $0.65\,\mathrm{V}$ to $0.50\,\mathrm{V}$ their values increase continuously, decreasing the homogeneity in the distribution consequently. The average power density obtained when the potential is set at $0.65\,\mathrm{V}$ ranges from $0.1190\ \mathrm{W\,cm^{-2}}$ to $0.2732\ \mathrm{W\,cm^{-2}}$ (see Table 3). These power densities are not the highest that can be achieved for the different cell configuration, due to the fact that this work aims to evaluate conditions that generate a more uniform current density, and thus a lower membrane degradation rate, while maintaining an adequate performance. For example, Xing et al. [27] work with power densities falling in the previously mentioned range. A reasonable trade-off between the average power density and an uniform current density is achieved at a $0.65\,\mathrm{V}$ potential. In light of this, the potential of $0.65\,\mathrm{V}$ is set in the cell to evaluate its performance under different operational and design conditions using the Taguchi experimental design.

5.2. Optimization at $0.65\,\mathrm{V}$

To perform the optimization using the Taguchi procedure, the mean power density data were normalized through the S/N_h ratio where "higher is better" (Eq. 21), and the roughness index was normalized with a S/N_l ratio where "lower is better" (Eq. 22) [6, 23, 41].

$$S/N_h(\bar{p}) = -10\log\left(\frac{1}{N}\frac{1}{\sum \bar{p}^2}\right) \tag{21}$$

$$S/N_l(\overline{ri}) = -10\log\left(\frac{1}{N}\sum \overline{ri}^2\right) \tag{22}$$

Table 3 shows the results of each simulation for a potential of $0.65\,\mathrm{V}$. The last two columns present the $\bar{p}$ normalized by the equation Eq. 21 and $\overline{ri}$ normalized by the Eq. 22.

Exp	$\bar{i}\ (\mathrm{A\,cm^{-2}})$	$\bar{p}\ (\mathrm{W\,cm^{-2}})$	CV(i)	Kur(i)	$\overline{ri}$	$CV(ri)$	$S/N_h(\bar{p})$	$S/N_l(\overline{ri})$
sim1111	0.2238	0.1455	0.493	-1.32	104.41	0.285	63.25	40.37
sim1222	0.4001	0.2601	0.046	-1.02	21.41	0.465	68.30	26.61
sim1333	0.4204	0.2732	0.024	-0.94	12.27	0.560	68.73	21.78

sim2123	0.3739	0.2430	0.068	-0.30	113.93	0.752	67.71	41.13
sim2231	0.4202	0.2731	0.029	-0.41	49.41	0.715	68.73	33.88
sim2312	0.2094	0.1361	0.630	-1.33	201.73	0.961	62.68	46.10
sim3132	0.4122	0.2680	0.045	4.62	92.80	0.991	68.56	39.35
sim3213	0.1830	0.1190	0.801	-1.52	202.09	0.700	61.51	46.11
sim3321	0.4162	0.2706	0.051	-0.74	44.64	0.621	68.64	32.99

Table 3: Comparison statistic indices for simulations at $0.65\,\mathrm{V}$.

	$S/N_h(\bar{p})$			
Parameter	*Lvl1*	*Lvl2*	*Lvl3*	$\Delta S/N_h$
Geometry (A)	66.76	66.37	66.24	0.53
Porosity (B)	66.51	66.18	66.68	0.51
Inlet vel.(C)	62.48	68.22	68.67	6.19
H_2O frac.(D)	66.87	66.51	65.98	0.89
	$S/N_l(\overline{ri})$			
				$\Delta S/N_l$
Geometry (A)	29.59	40.37	39.49	10.78
Porosity (B)	40.29	35.53	33.62	6.66
Inlet vel. (C)	44.19	33.58	31.67	12.52
H_2O frac. (D)	35.75	37.35	36.34	1.61

Table 4: Signal/noise ratio results by level and by parameter, for $\bar{p}$ in the upper part of the table and for $\overline{ri}$ in lower part of the table.

Table 4 shows the values of the normalized statistic indices averaged by level for each parameter, to analyze the sensitivity of the results. The last column presents the maximum difference between levels. The most sensitive parameters are those with the greatest difference between normalized values. In Table 4 it can be seen that the greatest influence on the net power density, is exerted by the inlet air velocity, followed by the vapor fraction, channel arrangement and lastly GDL porosity. The operating conditions with the highest generated power are those where S/N_h is maximized. The most favorable conditions to obtain the highest power density at

$0.65\,\mathrm{V}$ would be: parallel channel geometry (A1), high porosity (B3), maximum speed (C3) and the lowest vapor fraction in the inlet air flow (D1). In the case of $\overline{ri}$, working with the lower S/N_l ratio is better, because the lower it is, the more smoothly is the current density distributed on the active area. Table 4 shows that the velocity of the air, followed by the arrangement of the channels and GDL porosity have the greatest sensitivity on the current distribution ($\overline{ri}$). Again, the best results are presented by the geometries of parallel channels (A1), maximum porosity (B3), maximum speed (C3) and minimum vapor fraction (D1). Under these conditions (*sim1331*) and operating potential of $0.65\,\mathrm{V}$, the power would be brought to a maximum and the distribution of the locally generated current density would improve.

The operating conditions proposed in this work coincides with that of Lim et al. [42], where parallel channel arrangement present a lower pressure drop which favours the cell performance. A higher porosity improves the reactants access to the active surface which in turn promotes the current generation, as exhibited in Ref. Karthikeyan et al. [6], where a performance improvement is achieved increasing the porosity up to 0.65. Higher inlet air velocities lead to a higher power generation [42, 43]. This represents an improvement until the cell membrane dehydration starts to increase the ionic resistances.

In Fig. 7a and Fig. 7 the results of $\overline{p}$, $CV(i)$, $CV(ri)$ and $\overline{ri}$ for all the simulations determined with the Taguchi experimental design and *sim1331* (which was previously deemed as the best scenario) at $0.65\,\mathrm{V}$ are presented as a bar chart. In Fig. 7a, the $CV(i)$ axis tick labels are shown on the left and the simulation values are represented with red bars. The $\overline{p}$ axis tick labels are shown on the right side and the simulation values are represented with blue bars. Similarly, in Fig. 7 $\overline{ri}$ axis tick labels are shown on the left with its values in red bars, and the $CV(ri)$ labels are shown on the right and its values in blue bars.

In Fig. 7a it can be observed that six simulation show a high power density mean, from this simulations *sim1331* present the highest $\overline{p}$ value ($0.2745\,\mathrm{W\,cm^{-2}}$) and also the lowest CV(i). This low coefficient of variation indicates the low dispersion of the current density values.

In Fig. 7 for the $\overline{ri}$ values, three simulations have noticeably lower values than the rest, one of those being *sim1331*. For the $CV(ri)$ values, *sim1331* seems to be within the average. This results shows that the found combination of parameters responds appropriately.

[[Image]]

Figure 7: (a) Mean of power density ($\bar{p}$) and coefficient of variation of the current density ($CV(i)$) for the all the simulations. (b) Coefficient of variation of the roughness index ($CV(ri)$) and mean of the roughness index ($\overline{ri}$) for the all the simulations.

Fig. 8 shows the current density and roughness index over the active area for the simulation at the operating potential of $0.65\,\mathrm{V}$. On the left side, the current density over the active area is presented in the vertical axis. On the right side of the figure, the vertical axis is the ri index. Fig. 8a shows the results of *sim3213*. This simulation will be taken as a reference point since it is the one that gave the worst results. On the other hand, Fig. 8b shows the simulation (*sim1331*) with the optimal conditions at the operating potential of $0.65\,\mathrm{V}$. The ri presents a smooth surface, with only some points where it increases due to the decrease in current.

[[Image]]

Figure 8: (a) *sim3213* and (b) *sim1331* current densities (left) and ri (right).

Comparing the results of the simulation with the design parameters adjusted to the best conditions (*sim1331*) against the worst case scenario (*sim3213*), the power generated improves 2.31 times from $0.1190\,\mathrm{W\,cm^{-2}}$ to $0.2746\,\mathrm{W\,cm^{-2}}$. The coefficient of variation of the current density decreases from 0.80 to 0.02, the $\overline{ri}$ from 202.09 to 13.16 and the $CV(ri)$ from 0.70 to 0.61. These statistic indices reflect a more homogeneous distribution of locally generated current density. As can be seen in Fig. 8a and Fig. 8b the maximum current density for both simulations is within the same range but its distribution in the active area is not the same.

6. Conclusion

In this paper a simple half-cell model that provides information on the performance of a fuel cell under adequate anode conditions was successfully run. A novel method was proposed to interpret the current density distributions, using the roughness index. The indices $CV(i)$, $\overline{ri}$ and $CV(ri)$ provided a quantitative factor that can be used to compare the distribution at different variables over the active area. This model together with the proposed method provides a tool to identify and compare heterogeneities in the current density generated in the active area of the cell, while the Taguchi experimental design allows to optimize design parameters with a lower number of simulations. It could be determined that at high current demands, lower potential, a greater disparity is generated in the distribution of current density generated in the active area. A working potential that offers a good compromise between an homogeneous current density distribution and

a high power density was obtained. The best conditions under which the highest power density is developed for the selected potential were estimated, given by the higher porosity 0.6, the higher inlet air flow velocity of $6 m s^{-1}$, lower fraction of water in the inlet air flow of 0.10 and the parallel channels arrangement. The model presented in this work does not capture the behaviours of the water transport through the membrane nor its phase change. Despite this limitations, this results represent a first approach to find the cell conditions that guarantee a smooth distribution of current density, protecting the membrane from high degradation rates. A comparison of the results from the optimally selected design parameters against the results of the worst case simulated, shows a great improvement in all the studied statistic indices.

References

[1] A. Alaswad, A. Baroutaji, H. Achour, J. Carton, A. Al Makky, Developments in fuel cell technologies in the transport sector, International Journal of Hydrogen Energy 41 (37) (2016) 16499–16508, ISSN 0360-3199, doi:10.1016/J.IJHYDENE.2016.03.164, URL https://www.sciencedirect.com/science/article/pii/S0360319915315810.

[2] R. L. Borup, A. Kusoglu, K. C. Neyerlin, R. Mukundan, R. K. Ahluwalia, D. A. Cullen, K. L. More, A. Z. Weber, D. J. Myers, Recent developments in catalyst-related PEM fuel cell durability, Current Opinion in Electrochemistry 21 (2020) 192–200, ISSN 2451-9103, doi:10.1016/J.COELEC.2020.02.007, URL https://www.sciencedirect.com/science/article/pii/S2451910320300326.

[3] O. S. Ijaodola, Z. El-Hassan, E. Ogungbemi, F. N. Khatib, T. Wilberforce, J. Thompson, A. G. Olabi, Energy efficiency improvements by investigating the water flooding management on proton exchange membrane fuel cell (PEMFC), Energy 179 (2019) 246–267, ISSN 03605442, doi:10.1016/j.energy.2019.04. 074, URL doi:10.1016/j.energy.2019.04.074.

[4] T. Jahnke, G. Futter, A. Latz, T. Malkow, G. Papakonstantinou, G. Tsotridis, P. Schott, M. Gérard, M. Quinaud, M. Quiroga, A. A. Franco, K. Malek, R. F. D. Morais, T. Kerber, P. Sautet, D. Loffreda, S. Strahl, M. Serra, P. Polverino, C. Pianese, M. Mayur, W. G. Bessler, C. Kompis, F. Calle-Vallejo, R. Ferreira De Morais, T. Kerber, P. Sautet, D. Loffreda, S. Strahl, M. Serra, P. Polverino, C. Pianese, M. Mayur, W. G. Bessler, C.

Kompis, Performance and degradation of Proton Exchange Membrane Fuel Cells: State of the art in modeling from atomistic to system scale, Journal of Power Sources 304 (2016) 207–233, ISSN 03787753, doi:10.1016/j.jpowsour.2015.11.041, URL doi:10.1016/j.jpowsour.2015.11.041.

[5] T. Wilberforce, Z. El Hassan, E. Ogungbemi, O. Ijaodola, F. N. Khatib, A. Durrant, J. Thompson, A. Baroutaji, A. G. Olabi, A comprehensive study of the effect of bipolar plate (BP) geometry design on the performance of proton exchange membrane (PEM) fuel cells, Renewable and Sustainable Energy Reviews 111 (September 2018) (2019) 236–260, ISSN 18790690, doi: 10.1016/j.rser.2019.04.081, URL doi:10.1016/j.rser.2019.04.081.

[6] P. Karthikeyan, M. Muthukumar, S. V. Shanmugam, P. P. Kumar, S. Murali, A. P. S. Kumar, Optimization of operating and design parameters on proton exchange membrane fuel cell by using Taguchi method, Procedia Engineering 64 (2013) 409418, ISSN 18777058, doi:10.1016/j.proeng.2013.09.114, URL doi:10.1016/j.proeng.2013.09.114.

[7] H. Kahraman, M. F. Orhan, Flow field bipolar plates in a proton exchange membrane fuel cell: Analysis & modeling, Energy Conversion and Management 133 (2016) 363–384, ISSN 01968904, doi:10.1016/j.enconman.2016.10.053, URL https://www.sciencedirect.com/science/article/pii/S01968904 1630961Xhttp://linkinghub.elsevier.com/retrieve/pii/S019689 041630961X.

[8] N. J. Cooper, A. D. Santamaria, M. K. Becton, J. W. Park, Investigation of the performance improvement in decreasing aspect ratio interdigitated flow field PEMFCs, Energy Conversion and Management 136 (2017) 307–317, ISSN 01968904, doi: 10.1016/j.enconman.2017.01.005, URL doi:10.1016/j.enconman.2017.01.005.

[9] N. J. Cooper, T. Smith, A. D. Santamaria, J. W. Park, Experimental optimization of parallel and interdigitated PEMFC flow-field channel geometry, International Journal of Hydrogen Energy 41 (2) (2016) 1213–1223, ISSN 03603199, doi: 10.1016/j.ijhydene.2015.11.153, URL doi:10.1016/j.ijhydene.2015.11.153.

[10] W. Li, Q. Zhang, C. Wang, X. Yan, S. Shen, G. Xia, F. Zhu, J. Zhang, Experimental and

numerical analysis of a threedimensional flow field for PEMFCs, Applied Energy 195 (2017) 278–288, ISSN 03062619, doi:10.1016/j.apenergy.2017.03.008, URL doi:10.1016Zj.apenergy.2017.03.008.

[11] N. Ahmadi, S. Rezazadeh, A. Dadvand, I. Mirzaee, Study of the Effect of Gas Channels Geometry on the Performance of Polymer Electrolyte Membrane Fuel Cell, Periodica Polytechnica Chemical Engineering ISSN 03245853, doi:10.3311/PPch.9369, URL https://pp.bme.hu/ch/article/view/9369.

[12] R. Behrou, A. Pizzolato, A. Forner-Cuenca, Topology optimization as a powerful tool to design advanced PEMFCs flow fields, International Journal of Heat and Mass Transfer 135 (2019) 72–92, ISSN 00179310, doi:10.1016/j.ijheatmasstransfer.2019.01.050, URL doi:10.1016/j.ijheatmasstransfer.2019.01.050.

[13] B. Randrianarizafy, P. Schott, M. Chandesris, M. Gerard, Y. Bultel, Design optimization of rib/channel patterns in a PEMFC through performance heterogeneities modelling, International Journal of Hydrogen Energy 43 (18) (2018) 8907–8926, ISSN 03603199, doi:10.1016/j.ijhydene.2018.03.036, URL doi:10.1016/j.ijhydene.2018.03.036.

[14] H. Liu, P. Li, K. Wang, Optimization of PEM fuel cell flow channel dimensions Mathematic modeling analysis and experimental verification, International Journal of Hydrogen Energy 38 (23) (2013) 9835–9846, ISSN 03603199, doi:10.1016/j.ijhydene.2013.05.159, URL http://www.sciencedirect.com/science/article/pii/S0360319913013918.

[15] S. O. Obayopo, T. Bello-Ochende, J. P. Meyer, Modelling and optimization of reactant gas transport in a PEM fuel cell with a transverse pin fin insert in channel flow, International Journal of Hydrogen Energy 37 (13) (2012) 10286–10298, ISSN 03603199, doi:10.1016/j.ijhydene.2012.03.150.

[16] E. Testa, P. Maggiore, L. Pace, M. D. L. D. Vedova, P. Torino, M. D. L. Dalla Vedova, Sensitivity Analysis for a PEM Fuel Cell Model aimed to Optimization, WSEAS Transactions on Power Systems 10 (2015) 171–179, URL https://www.wseas.org/multimedia/journals/power/2015/a365816-098.pdf.

[17] M. Z. Chowdhury, O. Genc, S. Toros, Numerical optimization of channel to land width ratio for PEM fuel cell, International Journal of Hydrogen Energy 43 (23) (2018) 10798–10809, ISSN 03603199, doi:10.1016/j.ijhydene.2017.12.149, URL doi:10.1016/j.ijhydene.2017.12.149.

[18] B. Lim, E. Majlan, W. Daud, M. Rosli, T. Husaini, Numerical analysis of modified parallel flow field designs for fuel cells, International Journal of Hydrogen Energy 42 (14) (2016) 1–9, ISSN 03603199, doi:10.1016/j.ijhydene.2016.03.189, URL http://linkinghub.elsevier.com/retrieve/pii/S0360319915311630.

[19] S. Shimpalee, J. W. Van Zee, Numerical studies on rib & channel dimension of flow-field on PEMFC performance, International Journal of Hydrogen Energy 32 (7) (2007) 842–856, ISSN 03603199, doi:10.1016/j.ijhydene.2006.11.032.

[20] S. Lee, H. Jeong, B. Ahn, T. Lim, Y. Son, Parametric study of the channel design at the bipolar plate in PEMFC performances, International Journal of Hydrogen Energy 33 (20) (2008) 5691–5696, ISSN 03603199, doi:10.1016/j.ijhydene.2008.07.038.

[21] J. Lobato, P. Cañizares, M. A. Rodrigo, F. J. Pinar, E. Mena, D. Úbeda, Three-dimensional model of a 50cm2 high temperature PEM fuel cell. Study of the flow channel geometry influence, International Journal of Hydrogen Energy 35 (11) (2010) 5510–5520, ISSN 03603199, doi:10.1016/j.ijhydene.2010.02.089.

[22] G. M. Imbrioscia, H. I. Fasoli, Simulation and study of proposed modifications over straight-parallel flow field design, International Journal of Hydrogen Energy 39 (16) (2014) 8861–8867, ISSN 03603199, doi:10.1016/j.ijhydene.2013.11.079, URL http://linkinghub.elsevier.com/retrieve/pii/S0360319913028048.

[23] N. Solehati, J. Bae, A. P. Sasmito, Optimization of operating parameters for liquid-cooled PEM fuel cell stacks using Taguchi method, Journal of Industrial and Engineering Chemistry 18 (3) (2012) 1039–1050, ISSN 1226086X, doi:10.1016/j.jiec.2011.12. 003.

[24] B. Sezgin, D. G. Caglayan, Y. Devrim, T. Steenberg, I. Eroglu, Modeling and sensitivity analysis of high temperature PEM fuel cells by using Comsol Multiphysics, International Journal of Hydrogen Energy 41 (23) (2016) 10001–10009, ISSN 03603199, doi:10.1016/j.ijhydene.2016.03.142, URL

doi:10.1016/j.ijhydene.2016.03.142.

[25] O.-j. Kwon, H.-s. Shin, S.-h. Cheon, B. S. Oh, A study of numerical analysis for PEMFC using a multiphysics program and statistical method, International Journal of Hydrogen Energy 40 (35) (2015) 11577–11586, ISSN 0360-3199, doi: 10.1016/j.ijhydene.2015.03.163, URL doi:10.1016/j.ijhydene.2015.03.163.

[26] L. Xing, W. Shi, P. K. Das, K. Scott, Inhomogeneous distribution of platinum and ionomer in the porous cathode to maximize the performance of a PEM fuel cell, AIChE Journal 63 (11) (2017) 4895–4910, ISSN 00011541, doi:10.1002/aic.15826, URL http://doi.wiley.com/10.1002/aic.15826.

[27] L. Xing, Y. Wang, P. K. Das, K. Scott, W. Shi, Homogenization of current density of PEM fuel cells by in-plane graded distributions of platinum loading and GDL porosity, Chemical Engineering Science 192 (2018) 699–713, ISSN 00092509, doi: 699, URL 0'.

[28] R. D. G. González-Huerta, M. A. Leyva, G. Solorza-Feria, Estudio comparativo de la reducción electrocatalítica de oxígeno sobre rutenio y su desempenño en una celda de combustible con membrana polimérica, Journal of the Mexican Chemical Society 48 (2004) 1–6.

[29] L. You, H. Liu, A two-phase flow and transport model for the cathode of PEM fuel cells, International Journal of Heat and Mass Transfer 45 (11) (2002) 2277–2287, ISSN 00179310, doi: 10.1016/S0017-9310(01)00322-2.

[30] R. Girimurugan, P. Kishor Kumar, E. Manoj, D. Gowsal, P. Jayaprakash, Performance Analysis of PEM Fuel Cell with Six Pass Serpentine Flow Field under Various Operating Voltages, IJIRCT1201025 International Journal of Innovative Research and Creative Technology www.ijirct.org 100, ISSN 24545988, URL www.ijirct.org.

[31] D. G. Caglayan, B. Sezgin, Y. Devrim, I. Eroglu, Threedimensional modeling of a high temperature polymer electrolyte membrane fuel cell at different operation temperatures, International Journal of Hydrogen Energy 41 (23) (2016) 10060–10070, ISSN 0360-3199, doi:10.1016/j.ijhydene.2016.03.049, URL doi:10.1016/j.ijhydene.2016.03.049.

[32] F. Barbir, Fuel Cell Electrochemistry, in: PEM Fuel Cells, Elsevier, 33–72, doi:10.1016/b978-012078142-3/50004-5, 2005.

[33] I. Nitta, T. Hottinen, O. Himanen, M. Mikkola, Inhomogeneous compression of PEMFC gas diffusion layer: Part I. Experimental, Journal of Power Sources 171 (1) (2007) 26–36, ISSN 0378-7753, doi:10.1016/J.JP0WS0UR.2006.11.018, URL https://www.sciencedirect.com/science/article/pii/S0378775306023056.

[34] P. Ramesh, S. P. Duttagupta, Effect of channel dimensions on micro PEM fuel cell performance using 3D modeling, International Journal of Renewable Energy Research 3 (2) (2013) 353–358, ISSN 13090127, doi:10.20508/ijrer.81990.

[35] R. Byron Bird Warren E. Stewart Edwin N. Lightfoo, R. B. Bird, W. E. Stewart, E. N. Lightfoot, Transport Phenomena, Revised 2nd Edition, ISBN 0470115394, doi:10.1002/aic.690070245, URL http://www.amazon.com/exec/obidos/redirect?tag=citeulike07-20&path=ASIN/0470115394%0Ahttp://cw.wiley.com/WileyCDA/WileyTitle/productCd-0470115394.html, 2006.

[36] J. Bear, Y. Bachmat, J. Bear, Y. Bachmat, The Porous Medium, in: Introduction to Modeling of Transport Phenomena in Porous Media, Springer Netherlands, 3–42, doi:10.1007/ 978-94-009-1926-6{_}1, 1990.

[37] K. W. Lum, J. J. McGuirk, 2D and 3D Modeling of a PEMFC cathode with interdigitated gas distributors, Journal of the Electrochemical Society 152 (4), ISSN 00134651, doi:10.1149/1. 1869272.

[38] M. J. Kermani, D. G. Moghaddam, J. M. Stockie, A parametric study of cathode catalyst layer structural parameters on the performance of a PEM fuel cell, International Journal of Hydrogen Energy 35 (6) (2010) 2417–2427, ISSN 03603199, doi:10.1016/j.ijhydene.2009.12.111, URL doi:10.1016/j.ijhydene.2009.12.111.

[39] R. N. Kackar, Off-Line Quality Control, Parameter Design, and the Taguchi Method, Journal of Quality Technology 17 (4) (1985) 176–188, ISSN 0022-4065, doi:10.1080/00224065. 1985.11978964, URL https://www.tandfonline.com/doi/abs/10.1080/00224065.1985.11978964.

[40] Y.-X. Huang, C.-H. Cheng, X.-D. Wang, J.-Y. Jang, Effects of porosity gradient in gas

diffusion layers on performance of proton exchange membrane fuel cells, Energy 35 (12) (2010) 4786–4794, ISSN 03605442, doi:10.1016/j.energy.2010.09.011, URL doi:10.1016Zj.energy.2010.09.011%5Cnhttp://linkinghub.elsevier.com/retrieve/pii/S0360544210004901.

[41] S. Toghyani, S. Fakhradini, E. Afshari, E. Baniasadi, M. Y. Abdollahzadeh Jamalabadi, M. Safdari Shadloo, Optimization of operating parameters of a polymer exchange membrane electrolyzer, International Journal of Hydrogen Energy 44 (13) (2019) 6403–6414, ISSN 0360-3199, doi:10.1016/J.IJHYDENE. 2019.01.186, URL https://www.sciencedirect.com/science/article/pii/S0360319919303453.

[42] B. H. Lim, E. H. Majlan, W. R. W. Daud, T. Husaini, M. I. Rosli, Effects of flow field design on water management and reactant distribution in PEMFC: a review, Ionics (2016) 1–16ISSN 18620760, doi:10.1007/s11581-016-1044-y.

[43] P. K. Takalloo, E. S. Nia, M. Ghazikhani, Numerical and experimental investigation on effects of inlet humidity and fuel flow rate and oxidant on the performance on polymer fuel cell, Energy Conversion and Management 114 (2016) 290–302, ISSN 01968904, doi:10.1016/j.enconman.2016.01.075, URL doi:10.1016/j.enconman.2016.01.075.

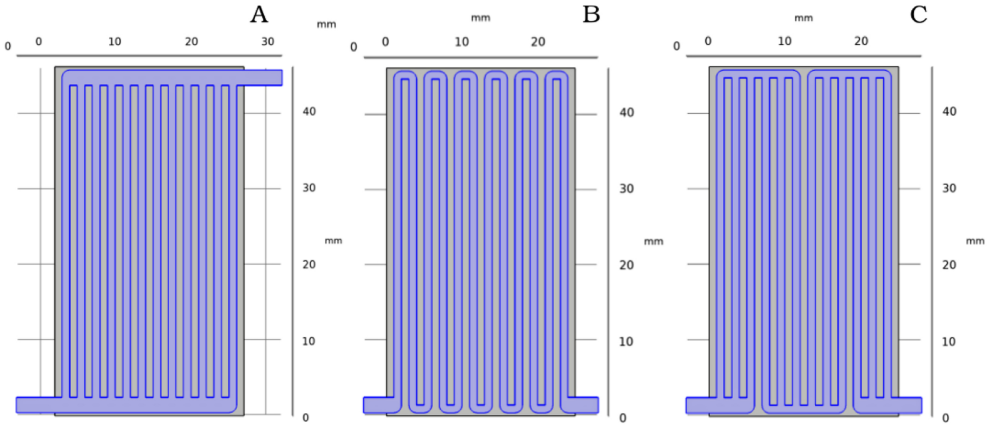

Figure 1

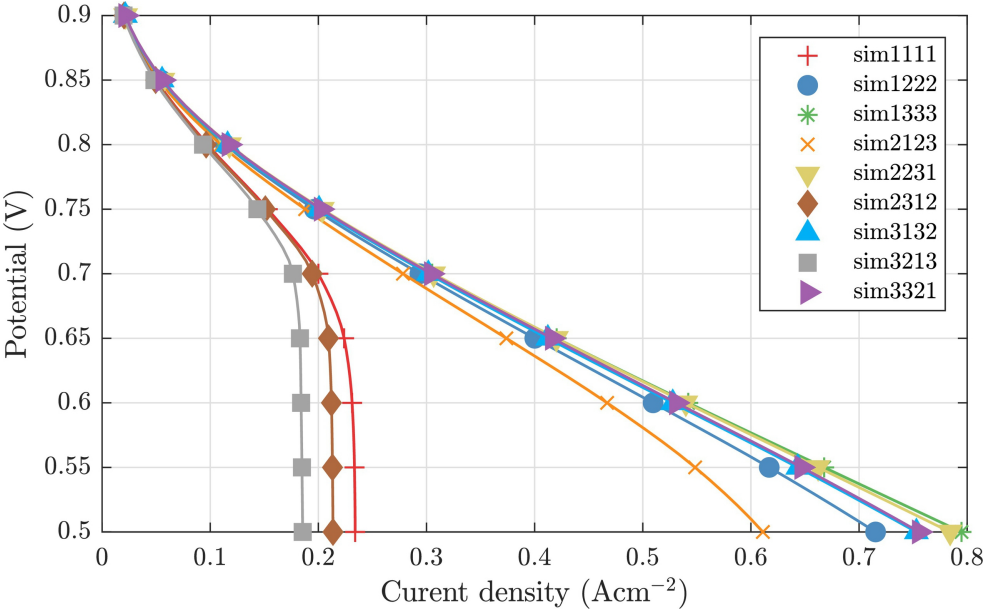
Potential (V)
0.9
0.85
0.8
0.75
0.7
0.65
0.6
0.55
0.5
0
0.1
0.2
0.3
0.4
0.5
0.6
0.7
0.8
Curent density (Acm^{-2})
sim1111
sim1222
sim1333
sim2123
sim2231
sim2312
sim3132
sim3213
sim3321

Figure 2

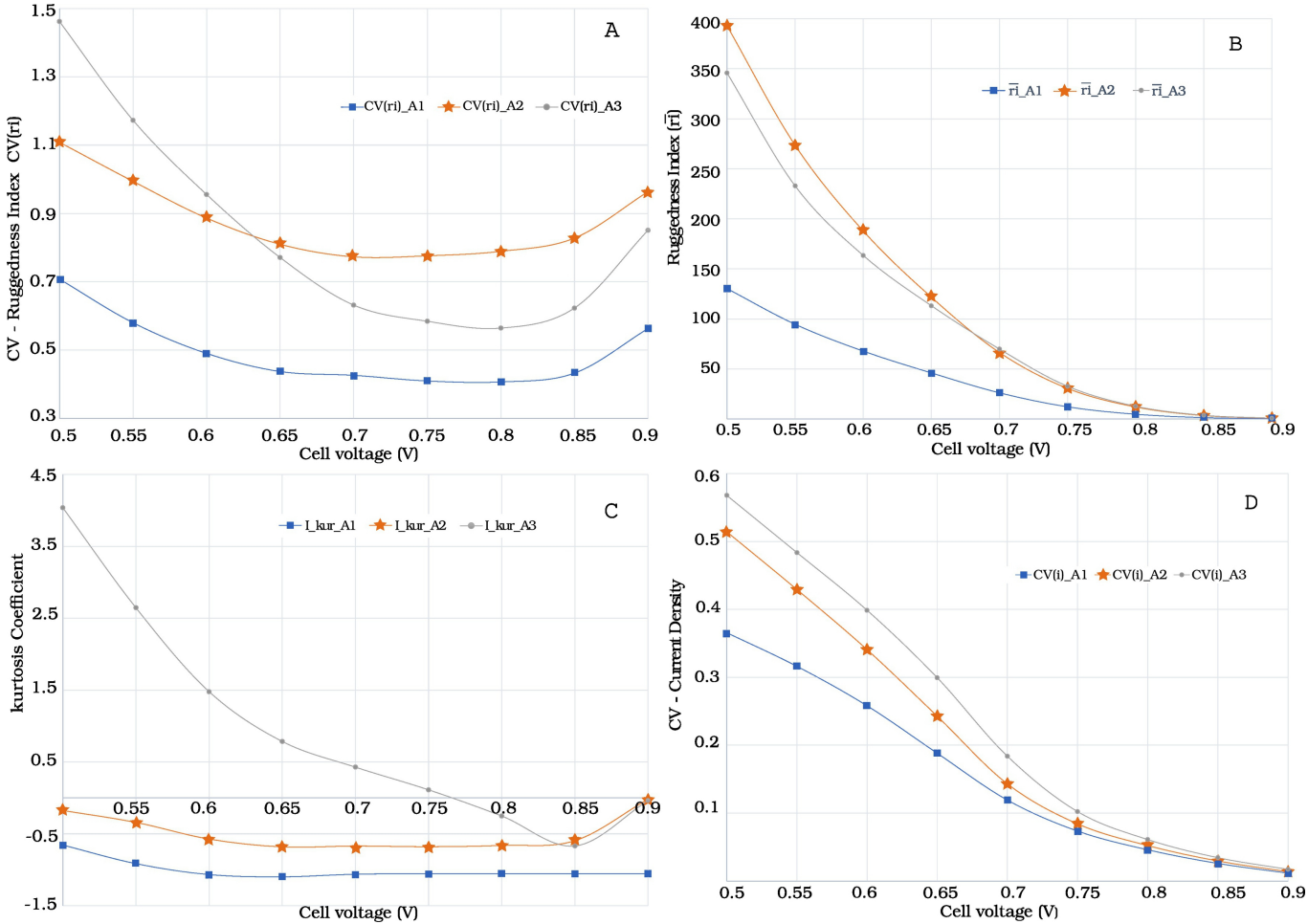
A
CV(ri)_A1
CV(ri)_A2
CV(ri)_A3
CV - Ruggedness Index CV(ri)
Cell voltage (V)
B
r̄i_A1
r̄i_A2
r̄i_A3
Ruggedness Index (r̄i)
Cell voltage (V)
C
I_kur_A1
I_kur_A2
I_kur_A3
kurtosis Coefficient
Cell voltage (V)
D
CV(i)_A1
CV(i)_A2
CV(i)_A3
CV - Current Density
Cell voltage (V)

Figure 3

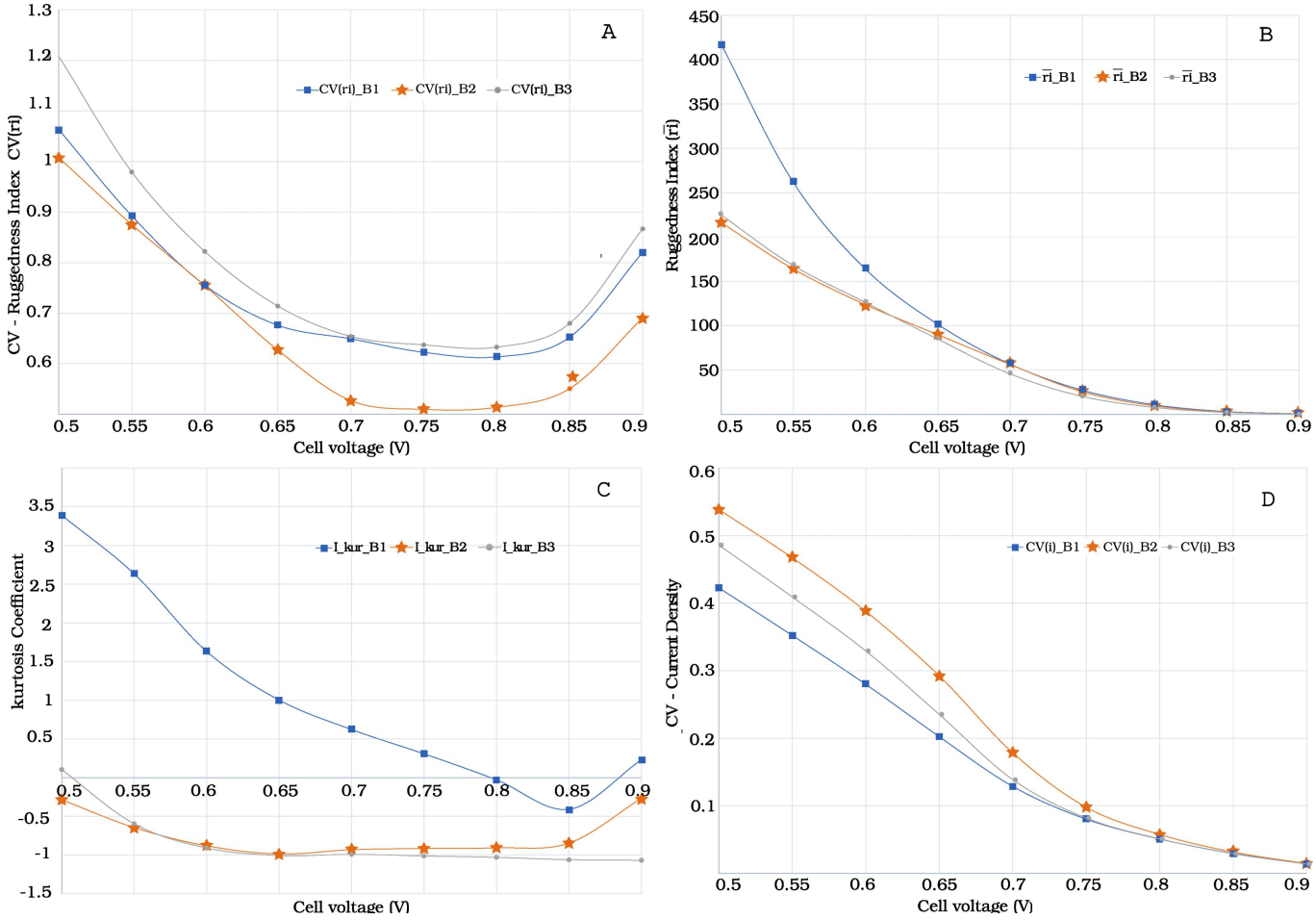
A
CV(ri)_B1
CV(ri)_B2
CV(ri)_B3
CV - Ruggedness Index CV(ri)
Cell voltage (V)
B
r̄i_B1
r̄i_B2
r̄i_B3
Ruggedness Index (r̄i)
Cell voltage (V)
C
I_kur_B1
I_kur_B2
I_kur_B3
kurtosis Coefficient
Cell voltage (V)
D
CV(i)_B1
CV(i)_B2
CV(i)_B3
CV - Current Density
Cell voltage (V)

Figure 4

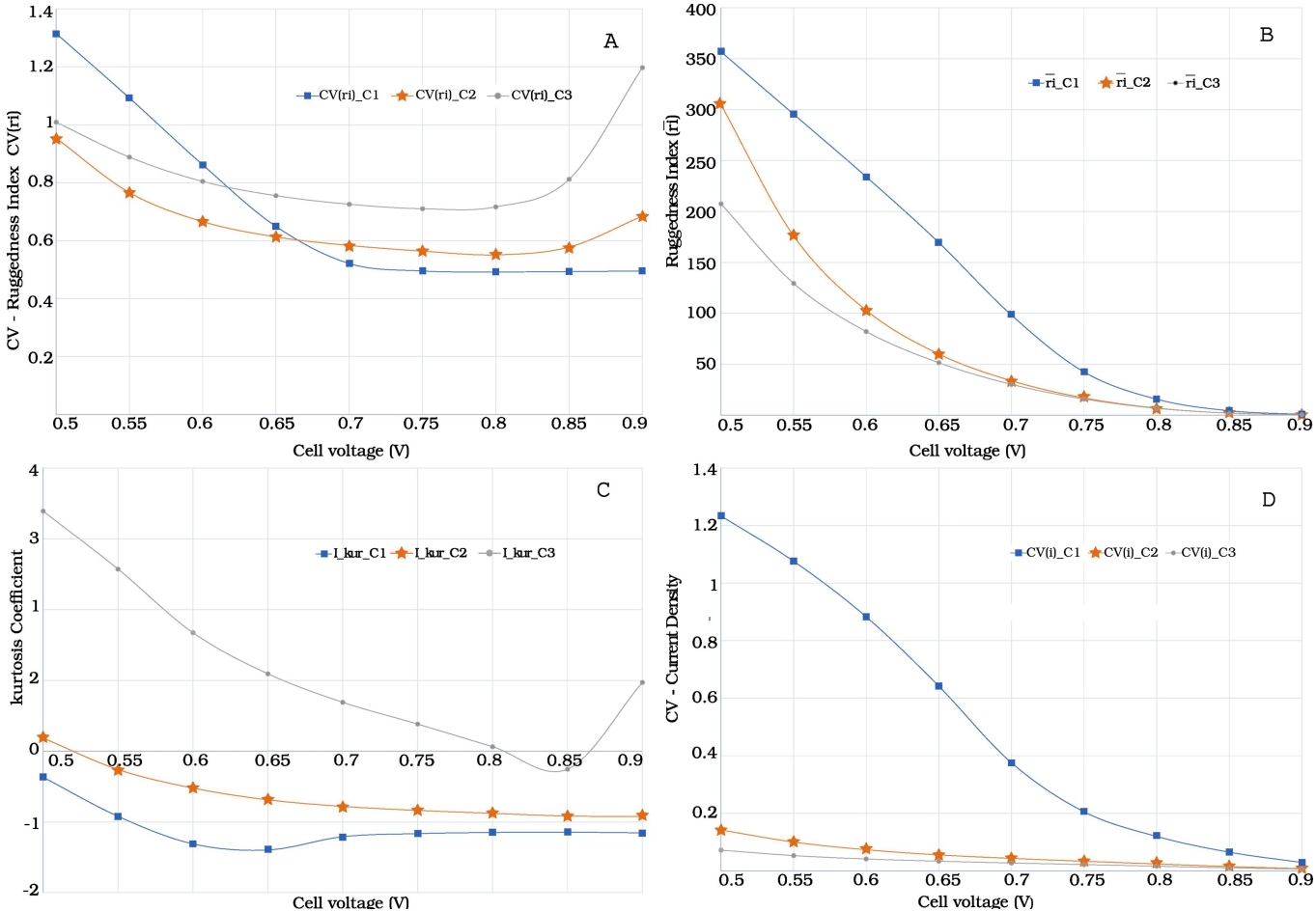
A
CV(ri)_C1
CV(ri)_C2
CV(ri)_C3
CV - Ruggedness Index CV(ri)
Cell voltage (V)
B
r̄i_C1
r̄i_C2
r̄i_C3
Ruggedness Index (r̄i)
Cell voltage (V)
C
I_kur_C1
I_kur_C2
I_kur_C3
kurtosis Coefficient
Cell voltage (V)
D
CV(i)_C1
CV(i)_C2
CV(i)_C3
CV - Current Density
Cell voltage (V)

Figure 5

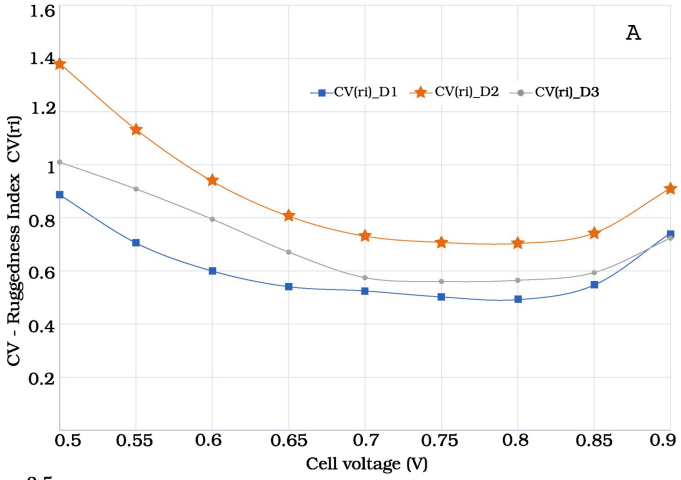
A
CV(ri)_D1
CV(ri)_D2
CV(ri)_D3
CV - Ruggedness Index CV(ri)
Cell voltage (V)

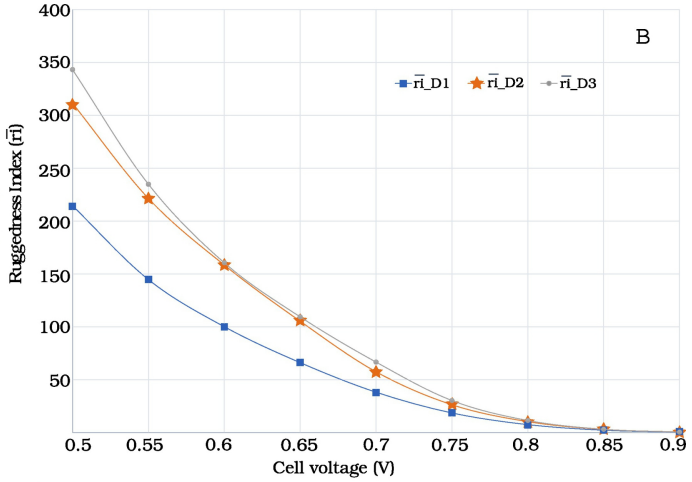
B
r̄i_D1
r̄i_D2
r̄i_D3
Ruggedness Index (r̄i)
Cell voltage (V)

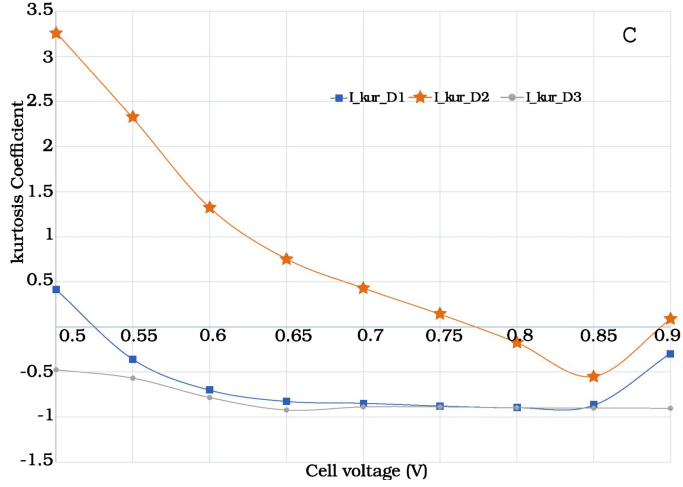
C
I_kur_D1
I_kur_D2
I_kur_D3
kurtosis Coefficient
Cell voltage (V)

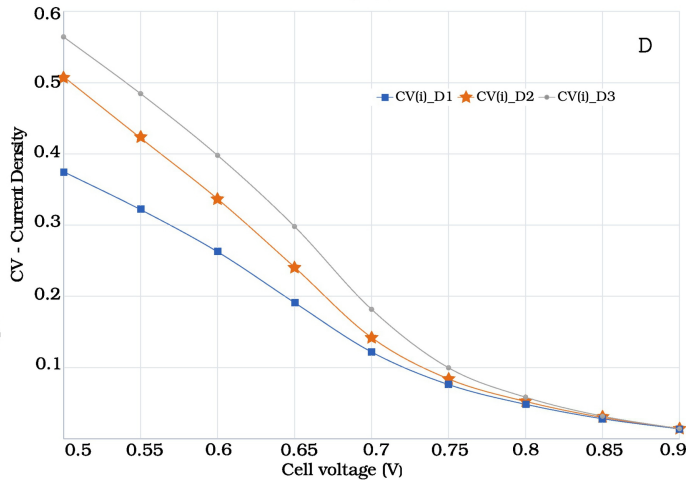
D
CV(i)_D1
CV(i)_D2
CV(i)_D3
CV - Current Density
Cell voltage (V)

Figure 6

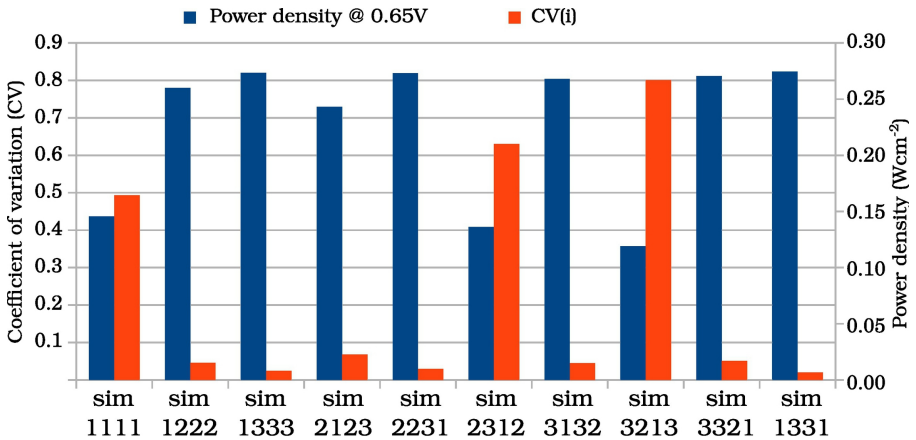
Power density @ 0.65V
CV(i)
Coefficient of variation (CV)
Power density (Wcm-2)
0.9
0.8
0.7
0.6
0.5
0.4
0.3
0.2
0.1
0.30
0.25
0.20
0.15
0.10
0.05
0.00
sim 1111
sim 1222
sim 1333
sim 2123
sim 2231
sim 2312
sim 3132
sim 3213
sim 3321
sim 1331

(a)

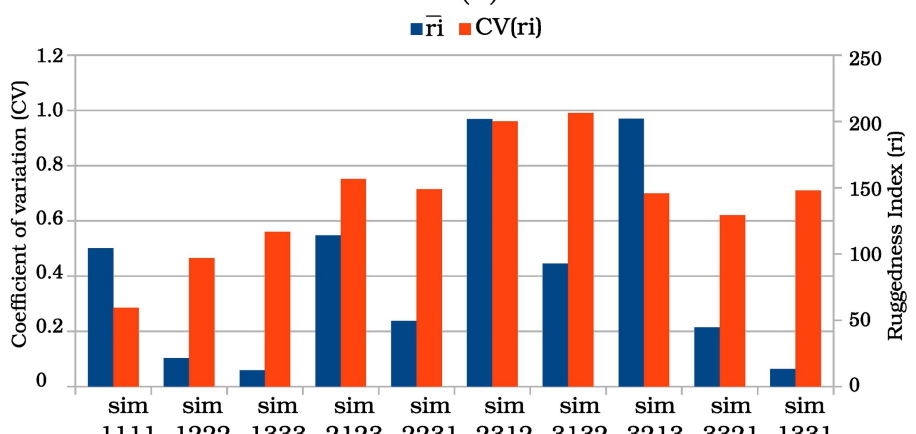
ri̅
CV(ri)
Coefficient of variation (CV)
Ruggedness Index (ri)
1.2
1.0
0.8
0.6
0.4
0.2
0
250
200
150
100
50
0
sim 1111
sim 1222
sim 1333
sim 2123
sim 2231
sim 2312
sim 3132
sim 3213
sim 3321
sim 1331

(b)

Figure 7

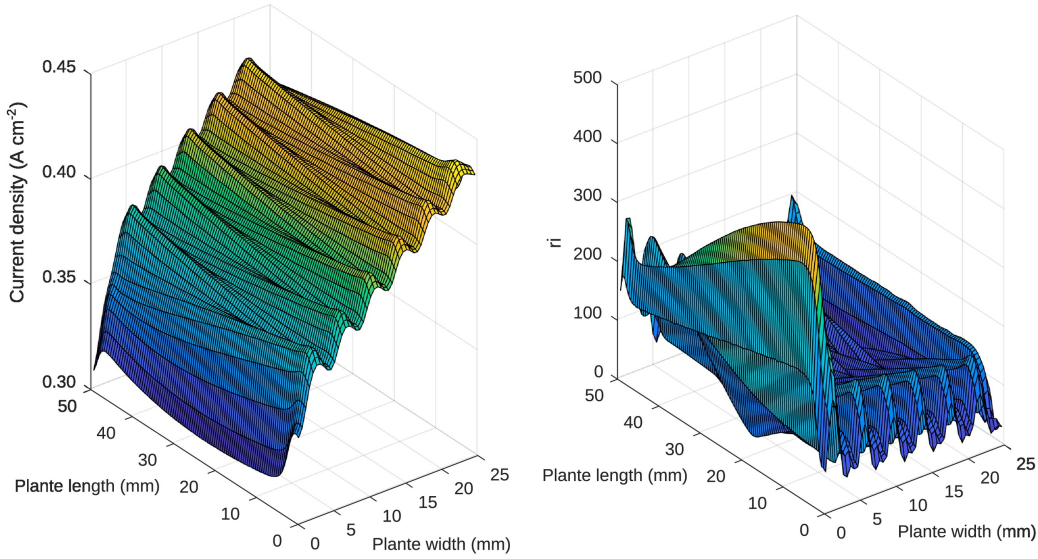
Current density (A cm-2)
0.45
0.40
0.35
0.30
Plante length (mm)
50
40
30
20
10
0
Plante width (mm)
0
5
10
15
20
25
ri
500
400
300
200
100
0
Plante length (mm)
Plante width (mm)

(a)

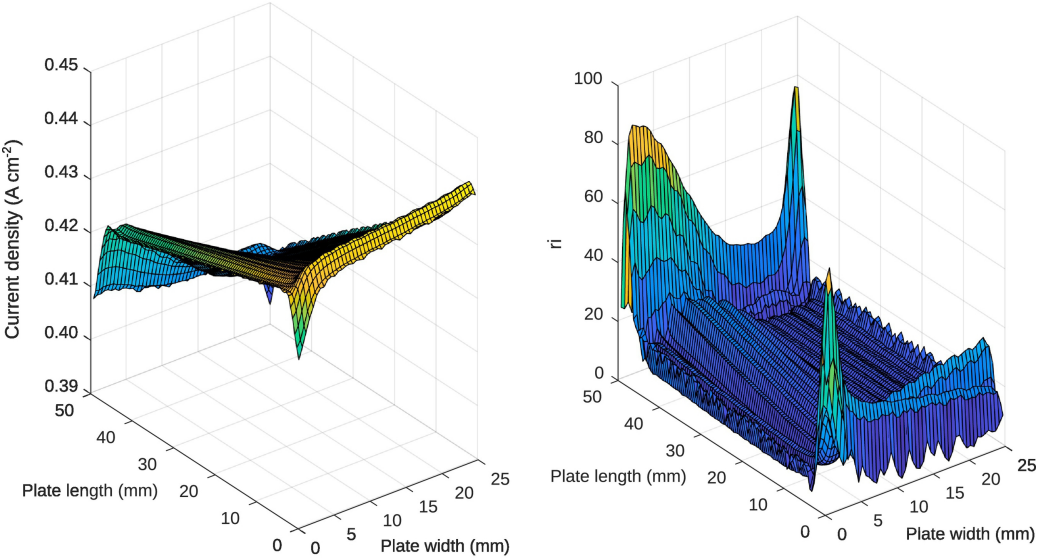
Current density (A cm-2)
0.45
0.44
0.43
0.42
0.41
0.40
0.39
Plate length (mm)
50
40
30
20
10
0
Plate width (mm)
0
5
10
15
20
25
ri
100
80
60
40
20
0
Plate length (mm)
Plate width (mm)

(b)

Figure 8